

Fully Synthetic 3D Fibrous Scaffolds for Stromal Tissues—Replacement of Animal-Derived Scaffold Materials Demonstrated by Multilayered Skin

Tobias Weigel,* Christoph Malkmus, Verena Weigel, Maximiliane Wußmann, Constantin Berger, Julian Brennecke, Florian Groeber-Becker, and Jan Hansmann

The extracellular matrix (ECM) of soft tissues in vivo has remarkable biological and structural properties. Thereby, the ECM provides mechanical stability while it still can be rearranged via cellular remodeling during tissue maturation or healing processes. However, modern synthetic alternatives fail to provide these key features among basic properties. Synthetic matrices are usually completely degraded or are inert regarding cellular remodeling. Based on a refined electrospinning process, a method is developed to generate synthetic scaffolds with highly porous fibrous structures and enhanced fiber-to-fiber distances. Since this approach allows for cell migration, matrix remodeling, and ECM synthesis, the scaffold provides an ideal platform for the generation of soft tissue equivalents. Using this matrix, an electrospun-based multilayered skin equivalent composed of a stratified epidermis, a dermal compartment, and a subcutis is able to be generated without the use of animal matrix components. The extension of classical dense electrospun scaffolds with high porosities and motile fibers generates a fully synthetic and defined alternative to collagen-gel-based tissue models and is a promising system for the construction of tissue equivalents as in vitro models or in vivo implants.

cellular intra- and interactions, tissue formation, the development of highly specific drugs against a variety of diseases, the assessment of novel treatment strategies for injuries, as well as the progression of implants such as advanced therapy medicinal products (ATMPs) are all prominent examples for the applicability of complex reconstructed tissues.^[1,2] Currently, the market for in vitro cell culture has a global annual size of 1.74 billion USD (2021) and an estimated compound annual growth rate (CAGR) of 10.7%.^[3] Furthermore, the market for cell-based therapies (ATPMs) has a size of 9.5 billion (2021) with a CAGR of 13.2%, wherein tissue-engineered products represent a share of around one third of the total value.^[4] At the present time, 3D-scaffold-based soft tissue products for in vitro and in vivo applications mainly rely or even exclusively depend on animal-derived materials.^[2] Besides the many justified advantages, increasing ethical

1. Introduction


In modern biomedical research, 3D cell and tissue culture has become indispensable for many years. The investigation of

and safety concerns as well as high production/standardization costs have resulted in a shifted demand of this market toward animal-free products.^[5] To address this development, constant efforts to improve synthetic and plant-based materials as well as their fabrication methods are necessary in order to serve the global demand for animal-free alternatives.

T. Weigel, V. Weigel, M. Wußmann, F. Groeber-Becker
Translational Center for Regenerative Therapies (TLC-RT)
Fraunhofer Institute for Silicate Research (ISC)
97082 Würzburg, Germany
E-mail: tobias.weigel@isc.fraunhofer.de

T. Weigel, C. Malkmus, V. Weigel, C. Berger, J. Brennecke,
F. Groeber-Becker, J. Hansmann
Department for Tissue Engineering and Regenerative Medicine
University Hospital Würzburg
97070 Würzburg, Germany

J. Hansmann
Faculty of Electrical Engineering
University of Applied Sciences Würzburg-Schweinfurt
97421 Schweinfurt, Germany

 The ORCID identification number(s) for the author(s) of this article can be found under <https://doi.org/10.1002/adma.202106780>.

© 2022 The Authors. Advanced Materials published by Wiley-VCH GmbH. This is an open access article under the terms of the Creative Commons Attribution-NonCommercial License, which permits use, distribution and reproduction in any medium, provided the original work is properly cited and is not used for commercial purposes.

DOI: 10.1002/adma.202106780

The classic elements in 3D tissue culture are specific scaffold structures as well as tissue-specific cells or related progenitor cells.^[6] Concerning the material part, the fundamental prerequisite for scaffolds is to provide structural support for cell attachment and subsequent tissue development in a specific 3D context.^[7] Decades of scientific developments have led to an enormous variety of scaffold materials and structures. To mimic the 3D stromal structure, the engineering of soft tissues currently utilizes scaffolds mainly based on animal-derived hydrogels such as collagen, gelatin and fibrin^[8–10] or decellularized organs.^[11,12] There are only a few synthetic alternatives, e.g., the commercial available, sponge-like membrane Alvetex.^[13,14] Nevertheless, this scaffold fails to mimic dermal fibrous structure and intrinsic flexibility. Further examples are highly defined synthetic hydrogels, that can mimic the extracellular matrix (ECM) on a molecular level leading to an exceptional control on several cellular functions such as adhesion and differentiation of complex cell types.^[15–17] However, high production costs and

finite mechanical stabilities due to missing fibril/fibrous structures limit the application domain of synthetic hydrogel-based tissues.

The design of new synthetic stromal scaffolds must address the relevant characteristics of the ECM *in vivo*. Fundamental and self-evident requirements are a suitable biocompatibility and surfaces facilitating cellular attachment, as well as a good availability and a high level of standardization. Concerning structural requirements, the scaffolds should provide mechanical stability to support handling during tissue preparation. Additionally, the scaffold's elasticity and flexibility^[18,19] needs to be set in the range of the desired tissue, with the possibility of slight adaptations by cellular interactions. The scaffold's structure requires an open porosity allowing cellular migration into the material and thereby fostering 3D of the tissue construct.^[20,21] Hence, pore sizes and pore walls need to be tailored to prevent a reduction to a convex 2D pore for the adherent cells. To mimic the fibrous structure of stromal ECM, the scaffold has to be assembled by fibers with physiological adjusted diameters in the sub-micrometer or nanometer range.^[22] In summary, the combination and translation of these structural features into a synthetic stromal scaffold are required to support the biological interactions. Besides cellular migration and the distribution of cells inside the entire scaffold, the structure must be adaptable for the applied stromal cells to facilitate remodeling processes. Precisely, fibroblasts move or digest fibers actively to alter the fibrous assembly at their discretion, comparable to natural fibril/fibrous scaffolds like collagen gels.^[23,24] Stromal tissue cells need to be stimulated to generate and deposit their own tissue-specific ECM as a biologically active fibrous network within the synthetic scaffold. Furthermore, the scaffold structure should facilitate cellular differentiation of distinct cell types during the stromal tissue maturation process.^[25,26]

To analyze the suitability of 3D scaffolds for functional stromal tissues, the engineering of skin tissue represents an ideal example. Anatomically, human skin is structured in three major tissue layers, the outer epidermis, followed by the underlying stromal layers specified as dermis and hypodermis. Human epidermal keratinocytes (heK) represent the major cell type of the epidermis that forms the barrier of the skin by a brick and mortar structure^[27] and require a defined surface to differentiate. The main component of the dermis is ECM such as fibrous proteins like collagen and elastin, produced by human dermal fibroblasts (hdF). The underlying hypodermis mainly consists of subcutaneous adipose tissue, a highly vascularized dynamic organ responsible for various functions such as energy storage, mechanical support, thermal insulation, endocrine function, and immunological processes.^[28–30] Due to the fibrous character of these two underlying stromal layers, they represent an appropriate application example for the suitability of stromal 3D scaffolds and the formation of a functional epithelium. Additionally, preceding approaches with animal-derived scaffolds demonstrated great challenges in generating multilayered skin equivalents, due to adverse cell-tissue-interactions, e.g., fibroblast-mediated collagen contraction^[31] or incompatibilities of different culture media formulations.^[32]

To address the requirements of synthetic scaffolds for the generation of stromal tissue, we used electrospun fibers due to their high availability, immense synthetic material variety

and appropriate fiber diameter.^[33] In our study, we improved the previous efforts to generate highly porous electrospun fiber scaffolds. We adapted a previously presented technique for the generation of defined 3D porous carbon fiber scaffolds^[34,35] to polymeric materials, whose mechanical properties are more similar to native stromal tissue and dramatically increased the porosity in the scaffold to address the defined requirements. To present the suitability of the developed highly porous electrospun fibrous scaffolds as stromal scaffolds, dermal tissues were generated and extended with a functional epidermis as well as a hypodermis. To investigate the relevance of the chosen material and scaffold structure, we tested two different fiber materials, polyamide 6 (PA6) and polycaprolactone (PCL), for their capability as a sufficient stromal 3D culture scaffold.

2. Results

2.1. Generation of Highly Porous Fibrous Scaffolds by Electrospinning

3D scaffolds for the generation of stromal tissues require excessively high porosities to enable a sufficient cellular migration and formation of specific ECM synthesized and deposited by the cells. With regard to electrospun meshes, the porosity needs to be achieved by the generation of pores inside the scaffold and by ensuring large-scaled mesh openings between the single pores. This can be achieved by a high amount of water soluble porogens, which separate fiber layers or even single fibers during scaffold synthesis and also ensure this highly porous structure after porogen removal in aqueous media (**Figure 1**).

In this study, 3D porous scaffolds were fabricated on a coaxial spinning setup by combination of electrospinning and embedding of NaCl porogens. By repeating short periods (3 min) of spinning procedures, the number of fibers placed on each other is limited and thereby the formation of inaccessible fiber layers is prevented. As scaffold materials, two prevalent polymers were applied to limit the cellular interactions to the improved structural properties: first, polyamide 6 (PA6), which is distinguished for its mechanical strength and stability against most organic solvents, allowing all standard biological characterizations. Second polycaprolactone (PCL) as one of the most applied polymers in the biomedical field, with biodegradable properties but less stability against organic solvents. SEM imaging of the scaffolds after spinning revealed embedded particles between the loose fiber network (**Figure 2A,B**) as well as the preferred fiber orientation caused by the rotation of the collector for both polymers. The fiber diameter was determined by imageJ and resulted in $371 \text{ nm} \pm 192 \text{ nm}$ for PA6 and $428 \pm 322 \text{ nm}$ for PCL. To remove the NaCl particles, scaffolds were subsequently placed in water (**Figure 2C**). Thereby, NaCl porogens dissolved rapidly and a half-transparent and floating scaffold remained. Due to the low extent of solid matter, the scaffold structure collapsed instantly after removal from the fluid and especially, when the scaffold dried the porosity was irreversibly lost. For this reason, all process steps needed to be performed under aqueous conditions, following the first contact with a liquid. By paraffin embedding and sectioning, the cross section on the PA6 scaffold showed a lamella-like structure

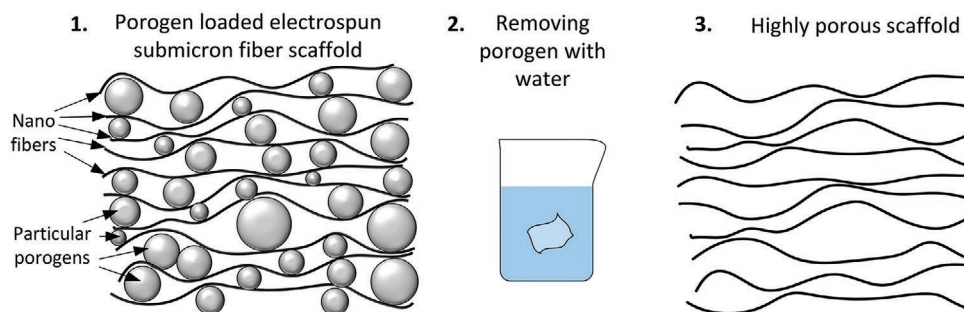


Figure 1. Approach for synthesis of highly porous fibrous scaffolds. In the first step, high amounts of particles (porogens) are embedded between the electrospun fibers during an electrospinning process (1). To achieve a highly porous scaffold, the particles were washed out by incubating the scaffold in water (2), and the porous fibrous structure remains (3).

with extended pores and a total thickness between 150 and 200 μm (Figure 2D). Based on scaffold thickness and weight, a porosity of $97.6 \pm 2.8\%$ could be calculated. Due to the incom-

patibility of PCL with paraffin embedding processes, a similar cross-sectional appearance as PA6 was assumed to the same fabrication procedure. To visualize the fiber mesh structure,

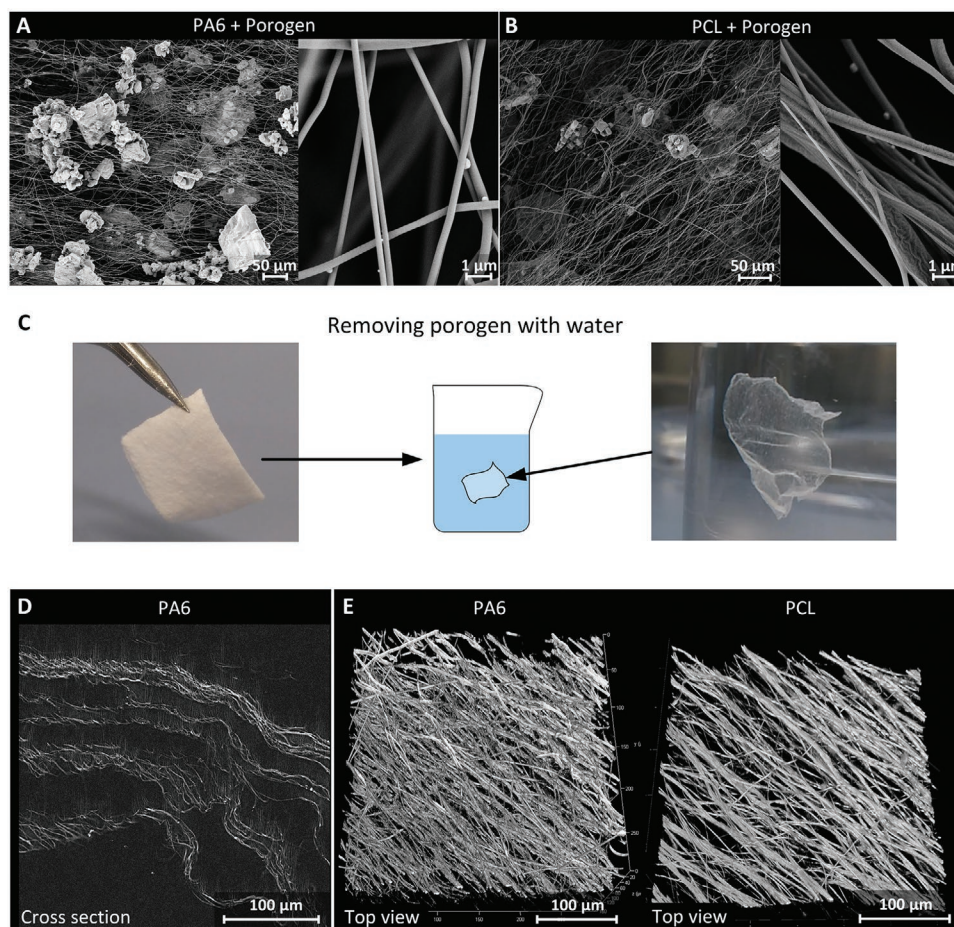


Figure 2. Structural characterization of the highly porous fibrous scaffolds. A,B) The combination of trapped NaCl particles and electrospun fibers is demonstrated in the left SEM image for PA6 (A) and PCL (B). Additional magnified SEM images on the right in (A) and (B) allow the fiber diameter determination with $371 \text{ nm} \pm 192 \text{ nm}$ for PA6 and $428 \pm 322 \text{ nm}$ for PCL (measuring 48 single fibers, respectively). C) To achieve a highly porous scaffold, the particles were washed out by incubating the scaffold in water. The resulting scaffold appeared half-transparent in the fluid. D) The lamina-like porous structure was imaged of a paraffin cross section of the PA6 scaffold by light microscopy (to visualize the fibers, the microscopy image was inverted and brightness/contrast enhanced). Additionally to the high amounts of pores, this fabrication technique increased the mesh openings within the fiber layers. E) Seen from the top by confocal reflection microscopy (Video S1, Supporting Information—PA6; Video S2—PCL), the increased fiber-to-fiber distances are visualized, that led to the increased mesh opening. The area of these meshes were quantified and provided in Figure S1 in the Supporting Information.

confocal reflection microscopy was applied, since this method can be performed directly in water. 3D-images showed an open fibrous structure with extended mesh openings and a certain fiber orientation similar for both materials (Figure 2E; Video S1, Supporting Information—PA6; Video S2, Supporting Information—PCL). The mesh openings in these images, measured by imageJ, ranged higher than $150 \mu\text{m}^2$ and a comparable size distribution of both materials (Figure S1, Supporting Information). Due to optical effects, fiber diameter appear thicker in confocal microscopy limiting the accuracy of the measurements.

2.2. Cellular Interactions and Biologization of the Synthetic Scaffolds

To examine the microscopic interaction of the highly porous PA6 scaffold with hdF as representative stromal tissue cells, the first fiber layer was recorded by confocal microscopy (around $50 \mu\text{m}$ z-stack) after 2 and 7 days of cell culture. During this culture, the scaffold was not mechanically fixed to allow movement of fibers in all directions. Floating was prevented by a metal ring. Imaging before cell seeding showed the loose fiber network (Figure 3A; Video S2, Supporting Information), with mesh openings ranging up to $150 \mu\text{m}^2$ and higher (Figure S1C, Supporting Information). After 2 days of culture, the cells populated the recorded fiber layer and interacted with the fibrous structure. As the fibers were moveable, the fibroblasts altered the scaffolds structure by pulling the single fibers toward the individual cells and thereby reduced the thickness of the fiber layer (Figure 3B; Video S3, Supporting Information) as well as shifted the mesh opening areas to higher values (Figure S1C, Supporting Information). Imaging after one week of culture indicated that the cells proliferated and populated the surface as well as the scaffold in the z-direction. To enable the insight into the scaffold, the upper dense cellular layer was partially faded out by the imaging software (Figure 3C; Video S4, Supporting Information). Additionally, the hdF contracted the scaffold in all directions, resulting in a condensed fiber network. It was no longer possible to distinguish between the fiber layers, indicating the loss of the fiber layers separating pores by the contraction forces of the cells. For the following experiments, the scaffolds were clamped into cell crowns^[36] to reduce tissue contraction in the horizontal direction and limit the contraction to the z-direction. For the formation of dermal connective tissue, the migration capability was first tested with hdF on the 3D scaffolds and on dense electrospun PA6 scaffolds. Immunohistological staining of paraffin sections showed a dense cell layer on top but no infiltration into the dense electrospun scaffold after two weeks (Figure 3D). In contrast, a complete populated scaffold was achieved by the mesh openings and high porosity for both materials. Based on the tissue depth and culture period a migration speed of $\approx 70 \mu\text{m}$ per week in z-direction (perpendicular to the main scaffold area) was estimated. Besides migration and proliferation, the synthesis of new ECM is a crucial step of biological tissue formation and maturation. To allow the secretion of collagen as the key protein in the dermal matrix hdF medium was supplemented with 100×10^{-6} and 500×10^{-6} M ascorbic acid 2-phosphate (Asc). Following two and four weeks, a hydroxyproline assay was performed to quantify

the synthesized collagen within the 3D scaffold (Figure 3E). After two weeks, collagen was hardly measurable with 100×10^{-6} M Asc. Higher culture durations of four weeks boosted the hydroxyproline content on PA6 to $0.25 \pm 0.08 \mu\text{g cm}^{-2}$. The supplementation of 500×10^{-6} M Asc increased the ECM secretion to a similar level already after two weeks of culture. In comparison, the detected amount of hydroxyproline on PCL was doubled in all experimental conditions, compared to the PA6 scaffolds. Due to the enhanced effectiveness of collagen production, a supplementation of 500×10^{-6} M Asc for two weeks was selected for further experiments.

The following experiments were performed exclusively with highly porous PA6 scaffolds and were repeated at the end on PCL in the supplement, to avoid overloaded figures. To assess the applicability of the 3D sub-micrometer fiber scaffold for the generation of an adipose tissue, the PA6 scaffold was seeded with human mesenchymal stromal cells (hMSCs). Staining of paraffin cross sections revealed the migration and proliferation of the cells throughout the complete scaffold (Figure 4A) with a decreased cell density compared to hdF. After two weeks of proliferation and migration, adipogenic differentiation was initiated by changing the culture medium to adipogenic differentiation medium (ADM). Two weeks later, an Oil red staining revealed the formation of lipid droplets inside the differentiating cells (Figure 4B). By expanding the differentiation to four weeks, the adipocyte density increased. Additionally, the quantity of lipid vacuoles per cell was reduced, whereas their volume increased (Figure S5B–D, Supporting Information). As an additional evidence for a successful adipogenic differentiation, an immunofluorescence staining against glucose transporter 4 (GLUT-4) showed an overall localization on the differentiating adipocyte membrane (Figure 4C) as well as the 3D embedding of these cells between the loose fiber network.

2.3. Mechanical and Micromechanical Properties of Highly Porous Electrospun Scaffolds

For the potential application as scaffold for skin equivalents, the mechanical properties of the highly porous PA6 fleeces were characterized in comparison to decellularized porcine skin tissue (dermis). Due to the low material density, tensile testing resulted in a 100-fold smaller Young's modulus and ultimate tensile stress (UTS) of the porous electrospun scaffold compared to native dermal tissue and also a substantial reduction compared to dense electrospun PA6 fleeces (Figure 5A,B). Biologization of the scaffold with hdFs ($+500 \times 10^{-6}$ M Asc) over 4 weeks and subsequent decellularization resulted in a mixed scaffold composed of PA6 fibers and ECM. This slightly increased the mechanical behavior in the stress–strain diagram (Figure S2A,B, Supporting Information), but did not lead to significant differences in the Young's modulus and UTS. Concerning the failure stretch ratio, the porous scaffolds showed a slight increase compared to dermal ECM and a dense fiber fleece. While tensile tests are quite useful to analyze the mechanics of a fully matured tissue compared to its native equivalent, microscopic mechanical characterizations are more important to estimate cellular interactions and for comparison to current hydrogel-based scaffolds.

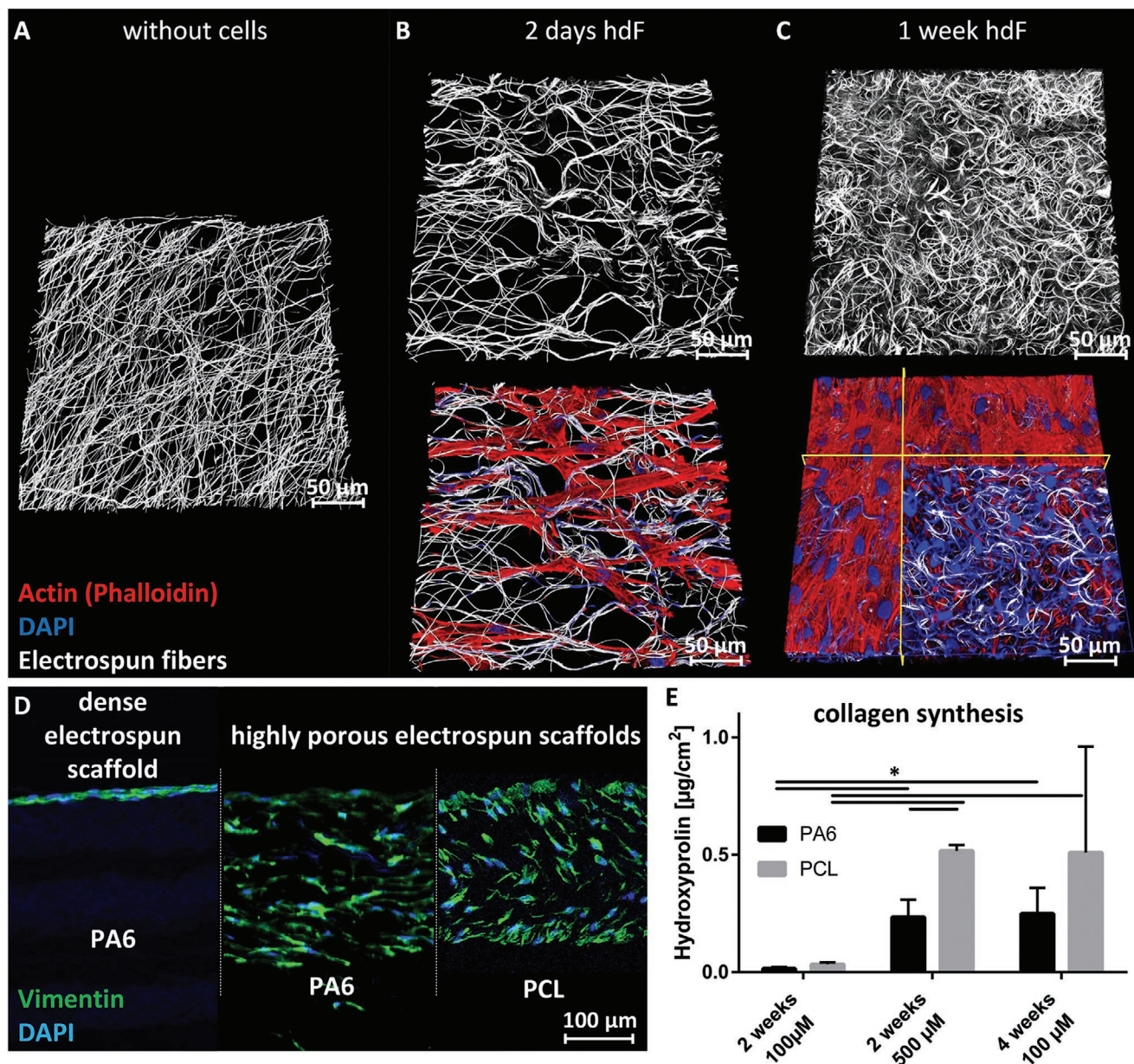


Figure 3. Interactions between human dermal fibroblasts and the porous fibrous structure—structural and biological scaffold remodeling. A) 3D image of the top fiber layer before cell seeding, recorded by confocal reflection microscopy. B) 3D images of the top fiber layer after 2 days incubation with 30 000 hdF cm^{-2} . The upper image displays the reflection signal of the fibers, the lower picture the overlay of the reflection, the actin skeleton of the hdF after fluorescence-coupled phalloidin staining and nucleus staining by DAPI. C) 3D images of the superficial scaffold region after 1 week of cell incubation. The upper image displays the reflection signal of the fibers, the lower picture the overlay of the reflection, the actin skeleton (phalloidin staining) and nucleus (DAPI). To visualize the structures below the dense superficial cellular layer, the upper few micrometers were removed by the rendering software in the area demarcated by the yellow marked section planes. For better 3D-visualization, all images are provided as videos in the supplements: A) Video S2, Supporting Information, (B) Video S3, Supporting Information, (C) Video S4, Supporting Information. Unfortunately, the interaction between the DNA-marker DAPI and the fibers increased with longer culture, leading to an overlaid signal of the fibers and the DAPI-positive cell nuclei. Therefore, the DAPI channel was removed in the last part of Video S4 in the Supporting Information. D) HdF cultured for 2 weeks on a dense and a highly porous electrospun scaffold, visualized by staining against vimentin. The dense electrospun fiber scaffold induced the formation of a cell layer on top, while the porous scaffolds of PA6 and PCL caused cell migration into the whole scaffold. E) ECM synthesis after two or four weeks with supplementation of 100×10^{-6} or 500×10^{-6} M Asc was measured by a quantitative hydroxyproline assay ($n = 3$); $*p < 0.05$.

Therefore, nanoindentation measurements including dynamic mechanical analysis (DMA) were performed to provide an insight in the relevant cellular-sized mechanical dimension. The porous PA6 scaffolds were seeded with hdF ($+500 \times 10^{-6}$ M Asc) to additionally observe mechanical remodeling. Due to the

extensive mesh openings, the indentation of a 50 μm sphere could not be performed on the pristine highly porous scaffold, but on the decellularized scaffold after 4 weeks of hdF culture. Determination of Young's modulus by nanoindentation revealed values of 456 ± 62 Pa for the decellularized porous scaffold

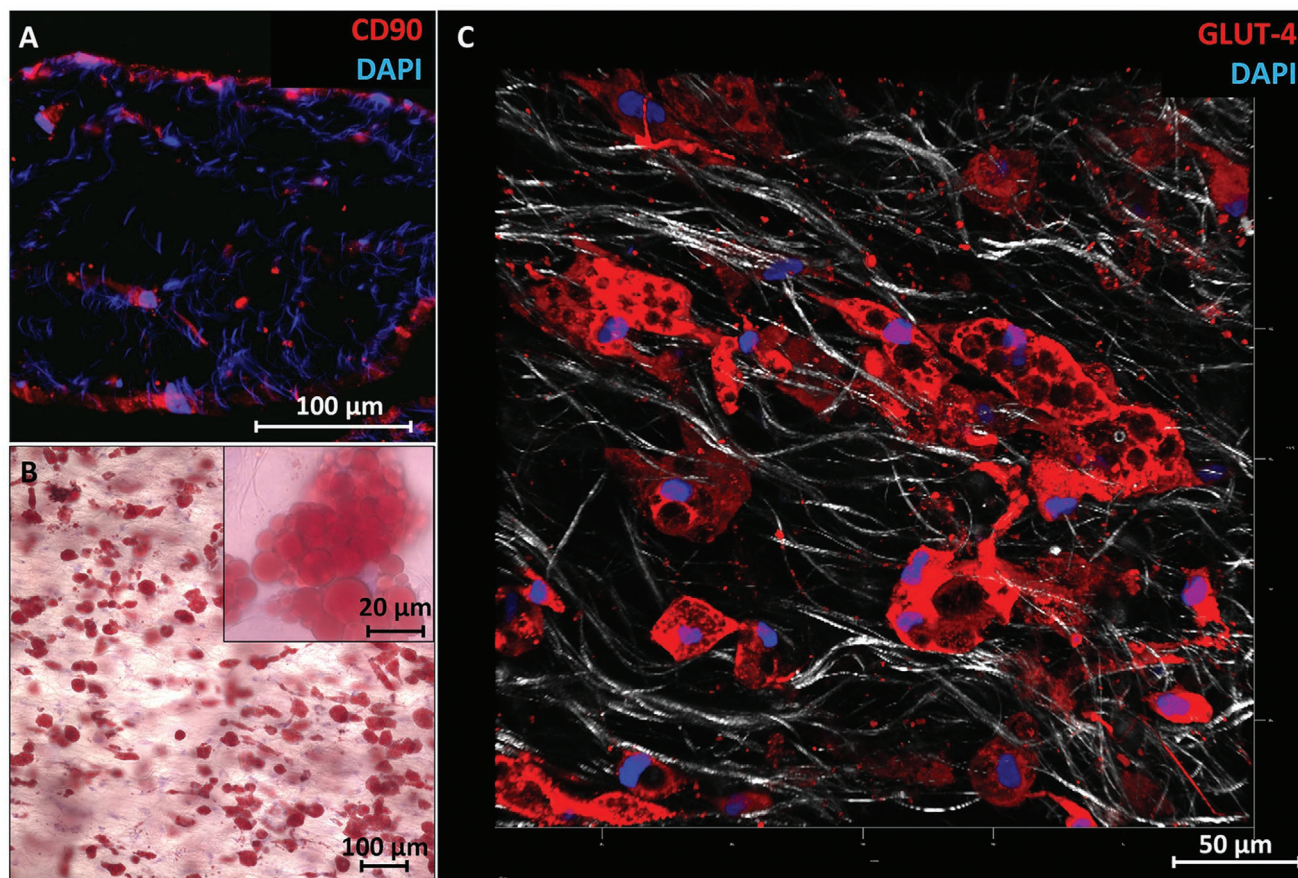


Figure 4. Migration and adipogenic differentiation of hMSC in the porous polyamide fiber scaffolds. A) Migration of hMSC in the porous scaffold visualized by fluorescent staining against CD90. B) Top view of Oil Red-positive adipogenic differentiating hMSCs in the porous scaffold after 2 weeks, with additional higher magnification in the inset. C) Confocal image after 4 weeks of adipogenic differentiation showing an antibody staining against GLUT-4 (red) and the polymer fibers by confocal reflection (gray).

(Figure 5C). Including cells, Young's modulus slightly rose after 1 week (nonsignificant, n.s.) and significantly increased one additional week later. After extended culture periods of 3 or 4 weeks, no further significant alterations were observed, indicating the formation of a multilayered cellular scaffold surface. For analysis of the viscoelastic properties of the biologized scaffolds, DMA in a range of 0.5–40 Hz was performed (Figure S3, Supporting Information). Similar to the Young's modulus, both, storage (E') and loss (E'') modulus significantly increased 2 weeks after hdF seeding and remained unchanged during extended culture. Interestingly, the dissipation factor ($\tan\delta = E''/E'$) slightly increased (n.s.) over time, indicating an elevation of viscous properties over culture time. In comparison to decellularized porcine skin and dense electrospun fibers, the biologized porous scaffolds exhibited a decreased stiffness as shown by lower Young's, storage and loss moduli (Figure S4, Supporting Information).

2.4. Biologized Fibrous Scaffolds as a Basis for Dermal Tissue for Skin Applications

The formation of a functional epidermis is one of the most important aspects in the generation of human skin equivalents.

For the dermal part, two scaffolds biologized by fibroblast (2 weeks culture, 500×10^{-6} M Asc) were combined by stacking, to increase the final thickness of the dermis. Afterward, the formation of the epidermis was started by seeding hEK onto the dermal part and culturing the construct under air lift conditions. After three weeks of maturation, the resulting electrospun-fiber-based skin model was analyzed. When removing the tissue model from the cell crown (Figure 6A), an increased mechanical stability compared to the initial scaffolds was noticeable when handling the constructs with tweezers. Hematoxylin–eosin (H&E) staining showed a well matured epidermis with all characteristic layers (Figure 6B). In the dermal part, the 4 stacked scaffolds fused together, forming a mechanically stable unit. Additionally, the dermal thickness of around 300 μm instead of 800 μm (four scaffolds with each 200 μm thickness initially) and the disappearance of the scaffold pores indicate a hdF-mediated contraction process during the epidermal maturation, which is already known for collagen-hydrogel-based skin models.^[27] Further analysis of the dermal part included immunofluorescence staining against vimentin and collagen I. In the dermis, vimentin acts as a specific marker for hdF and demonstrated a homogeneous distribution of the cells (Figure 6C) as already indicated in the H&E-image. A higher magnification indicates that the

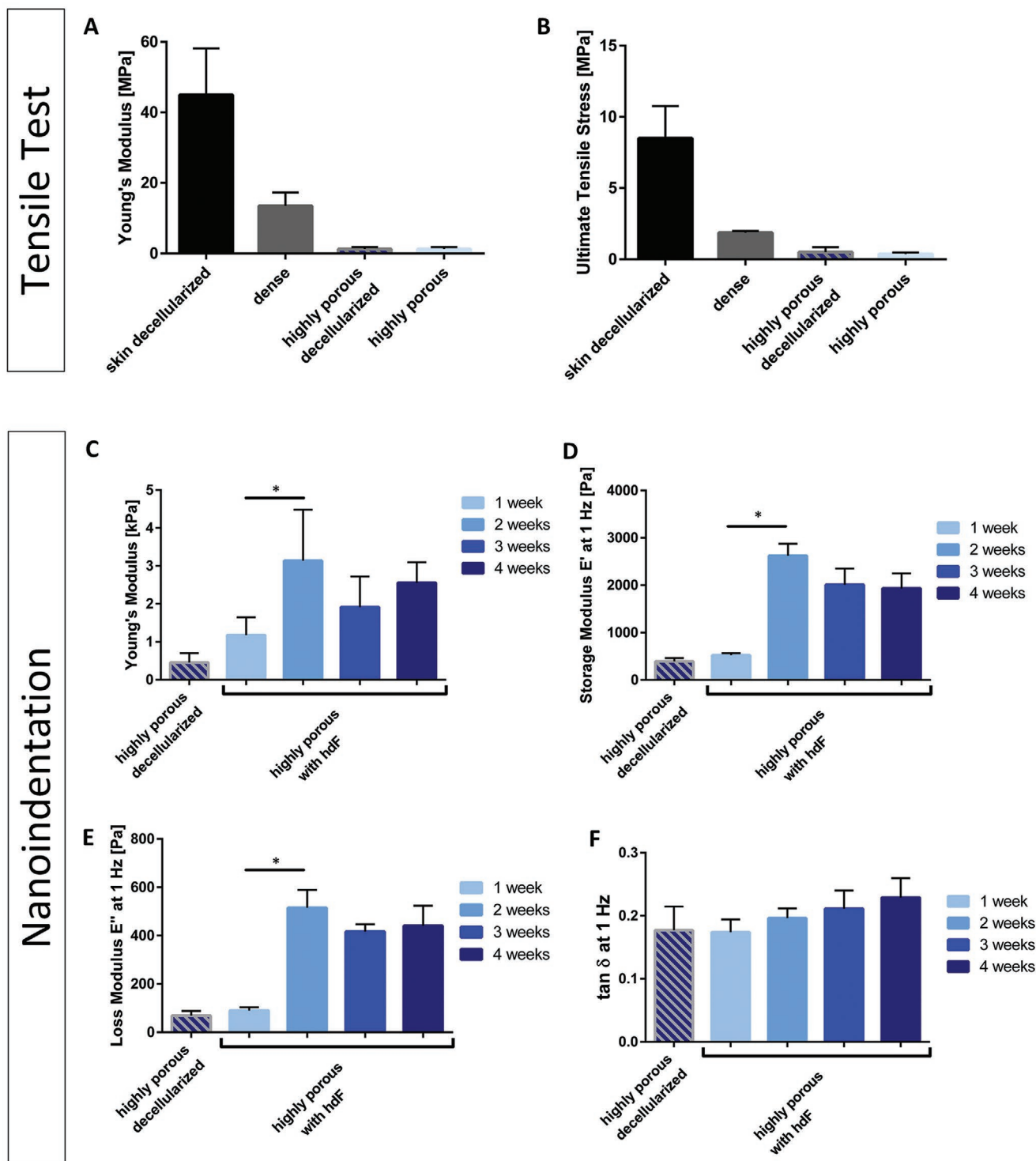


Figure 5. Mechanical characterization of highly porous PA6 scaffolds and comparison with dense electrospun scaffolds as well as decellularized porcine skin. For tensile tests, decellularized biologized highly porous scaffolds (4 weeks culture of hdF with 500 μm Asc) were included to examine the influence of ECM. All tensile measurements were performed in $n = 4$. A) Tensile modulus was determined in the linear region of the stress–strain diagram (Figure S2A,B, Supporting Information). B) The ultimate tensile stress was defined as the maximum tension. To observe the biologization process, nanoindentation measurements were performed weekly after seeding hdF on highly porous PA6 scaffolds. C) Evaluation of Young's modulus was performed by hertz fitting 9 indentation measurements of one sample (skin decellularized/dense) and 3 samples of all porous groups. D–F) Viscoelastic parameters were calculated from dynamic mechanical analyzes (DMA) by the nanoindentation software DataViewer ($n = 9$).

fibroblasts mainly attached to the fiber network. Staining against collagen I revealed a dense network of newly synthesized ECM

all over the 3D fiber scaffold (Figure 6D). A higher magnification showed the location of the collagen matrix, which filled

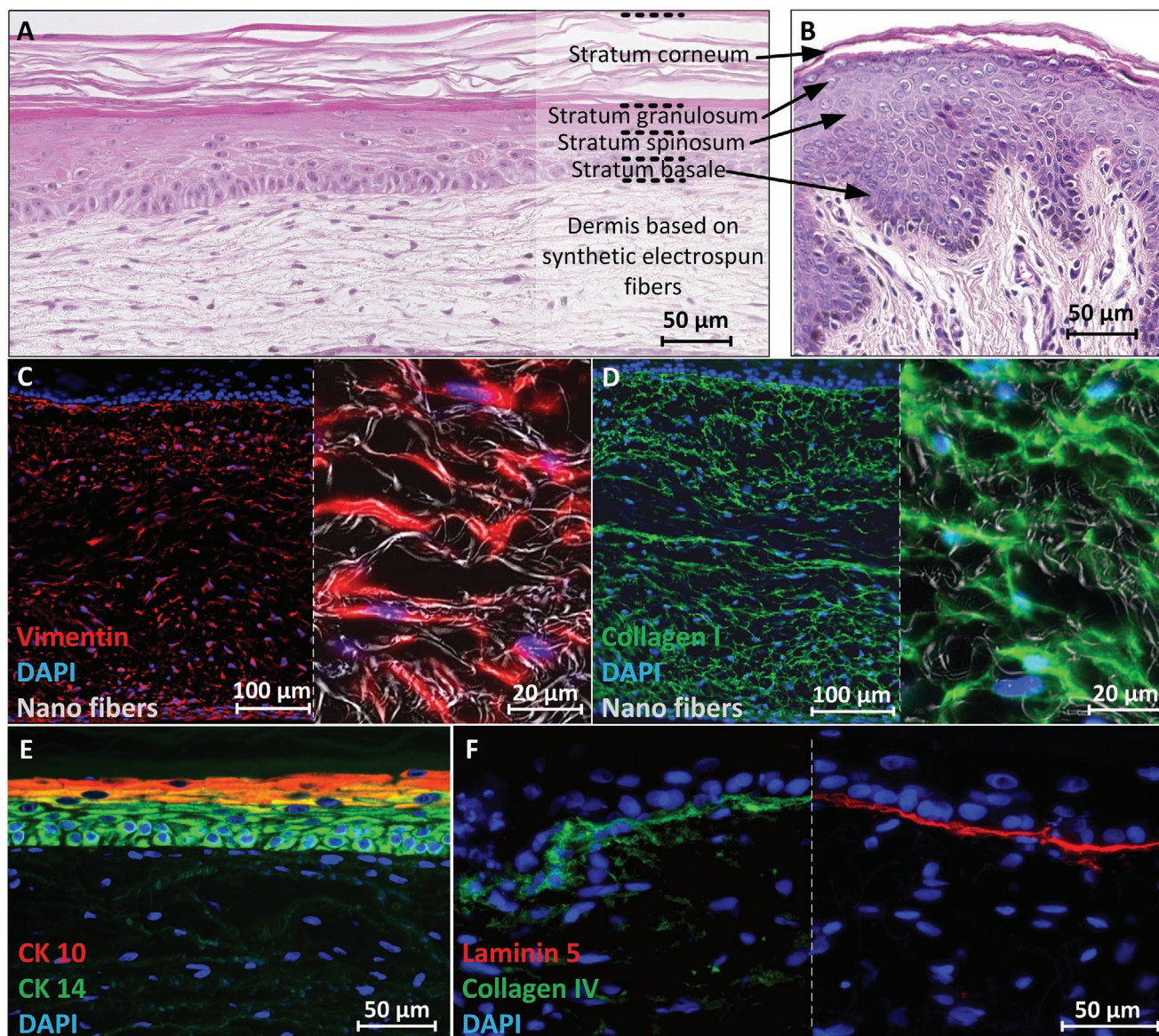


Figure 6. Generation of a two-layered skin model (dermis and epidermis) based on the highly porous PA6 fiber scaffolds. A) H&E staining of the electrospun 3D scaffold based skin model displays the characteristic layers of dermal skin tissue. B) H&E staining of native human skin demonstrates a similar structured epidermis additional with its typical papillary structure. C) Visualization of hdF distribution in the dermis by immunofluorescence staining against vimentin. The higher-magnification inset uncovers the location of the cells in comparison to the sub-micrometer fibers. To visualize these fibers, a bright-field image was inverted followed by sharp increase of brightness and contrast. D) Biologization of the porous fibrous scaffold part (dermal part) by hdF-mediated ECM synthesis was proven by immunofluorescence staining against collagen I and the cell nuclei with DAPI. Higher magnification of the collagen I staining (inset) shows the matrix distribution within the scaffold pores. E) Immunofluorescent (IF) staining against cytokeratin 14 and 10 demonstrates the differentiation status of the heK in the different epidermal layers. F) Staining of the basal lamina proteins laminin 5 and collagen IV.

the space in between the pores and the mesh openings of the synthetic scaffold. Immunofluorescence staining against Ki67 showed no proliferating cells (Figure S5A, Supporting Information), indicating a steady state within the 3D dermal tissue. Solely at the bottom of the dermal part, where hdF migrated out of the scaffold, and in the epidermal stratum basale, Ki67 positive cells were found. The immunofluorescent staining against cytokeratin 14 and 10 proved the differentiation-specific distribution of these proteins in the stratum basale, spinosum, and granulosum (Figure 6E). A functional unit of dermis

and epidermis is the delimiting basal membrane between these layers. Presence of the major basal membrane proteins laminin 5 and collagen IV (Figure 5F) located at the border between dermis and epidermis implies the formation of this membrane by the keratinocytes.^[37]

The barrier properties against outside influences is the main function of the epidermis. A nondestructive method to quantify this barrier is impedance spectroscopy, which requires a complete closed surface of the tissue. The cross section of an electrospun-fiber-based skin equivalent in Figure 7A

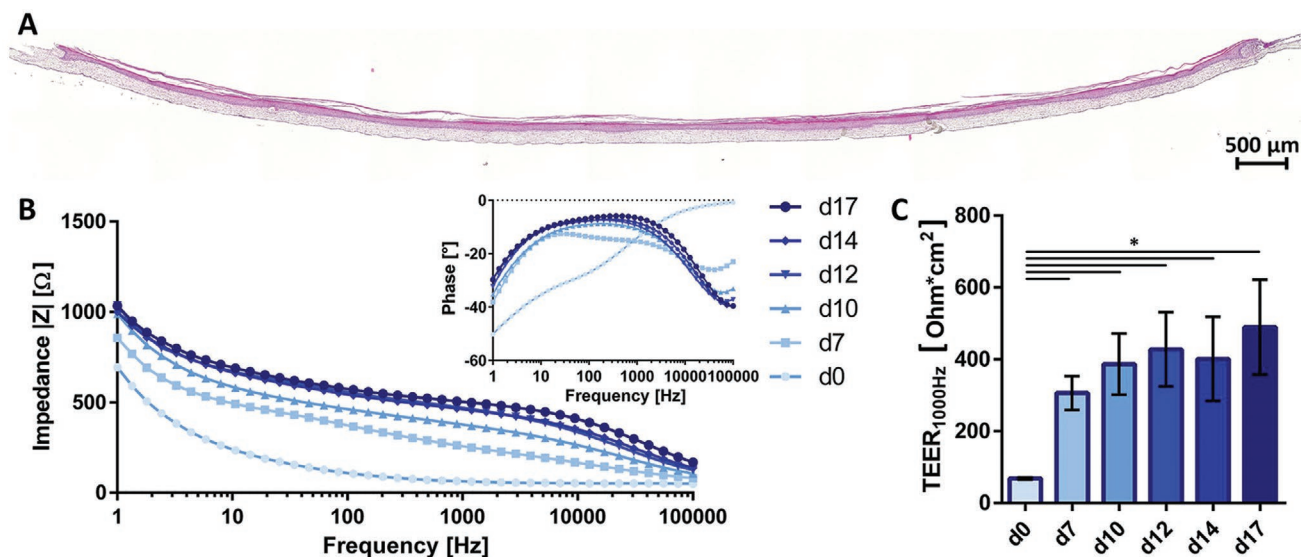


Figure 7. Barrier functionality by impedance spectroscopy. A) H&E-stained cross section of a complete electrospun-fiber-based skin equivalent. B) Development of the impedance and phase shift during the epidermal maturation progression. C) The increase of the TEER value describes the development of the characteristic epidermal barrier functionality ($n = 3$); $*p < 0.05$.

demonstrates the seamless closure even to the edges of the insert by the matured epidermis. This feature allowed a monitoring of the epidermal maturation by impedance spectroscopy. On day 0, the fibroblast seeded scaffold showed almost no electrical resistance against alternating currents (Figure 7B,C). After seeding heK, the impedance spectrum as well as the phase shift (Figure 7B inset) increased distinctly during culture. Further maturation processes between day 7 and 17 further increased the impedance values and thereby the barrier function. The epithelial barrier properties were quantified by the transepithelial electrical resistance (TEER_{1000Hz}) located at a frequency of 1000 Hz (Figure 6C), where the most prominent differences occur during epidermal differentiation and maturation.^[38] The TEER_{1000Hz} values started with $68.04 \pm 2.68 \Omega$ on day 0, increased distinctly to $306.16 \pm 38.33 \Omega$ on day 7 and further (but not significantly) to $437.49 \pm 107.88 \Omega$ on day 17.

2.5. Extension of Synthetic Fibrous-Based Skin Equivalent by an Adipose Tissue Layer

For the three-layered skin equivalent, both previously described tissues—the dermal part carrying a stratified epithelium and the 3D adipose tissue—were combined into one unit (Figure 8A). For this, two scaffolds of differentiating adipocytes (three weeks differentiation) were clamped under an unmaturing fiber-based skin model (1 week after heK seeding) and cultured for three weeks. During this time the adipocytes further matured, indicated by an increase of oil droplet size and the reduction of the oil droplet number within the cells (Figure 8B), confirmed over a time frame of six weeks. Interestingly, after a pre-differentiation of the hMSCs with ADM for three weeks, cell differentiation/maturation was even possible with the applied keratinocyte medium. Between week 2 and 6, the average oil droplet size increased from around 6.4 ± 4.5 to $24.6 \pm 3.9 \mu\text{m}$. The

increasing error bars indicate the formation of even bigger oil droplets (up to $50 \mu\text{m}$), but also the presence of at least one few-micrometer-sized droplet per pre-adipocyte. In contrast to the droplet size, the droplet number decreased during maturation from around 28.5 ± 11 to 3.9 ± 1.5 oil droplets per cell. Exemplary images with lower magnifications to the described time points are provided in the supplements (Figures S5B–D, Supporting Information).

Considering the dermal layer, paraffin cross sections of the electrospun-fiber-based three-layered skin equivalent (Figure 8C) showed similar characteristics as found in the two-layered model (Figure 3). However, the dermal part demonstrated a shrinkage to around $150 \mu\text{m}$ thickness. Below the dermal compartment, the adipose tissue layers were characterized by a decreased cell density and numerous cavities, representing the lipid vacuoles. To note, the lipids were removed during the paraffin embedding in the ascending alcohol series. To preserve the lipids in the tissue, additional models were cryo-sectioned and stained with Nile Red together with immunofluorescence against vimentin. Microscopy clearly showed the stained lipid-containing cells in red in the lower part of the tissue model (Figure 8D). The vimentin staining indicated a migration of hdF from the dermal part to the lower subcutaneous compartment which induced its contraction. Additionally, the hdF seemed to fuse both tissue layers to a mechanically stable unit. A further combined HE and Oil Red staining of the cryo-sections revealed a high number of stained oil droplets with a variety of sizes within the adipocytes (Figure 8E). Interestingly, this staining combination also enabled the detection of the lipids located in the stratum corneum (Figure 8F).

2.6. Material Variation of Highly Porous Fibrous Scaffolds

As biodegradability is an important issue in the development of tissue implants, the generation of two- and three-layered

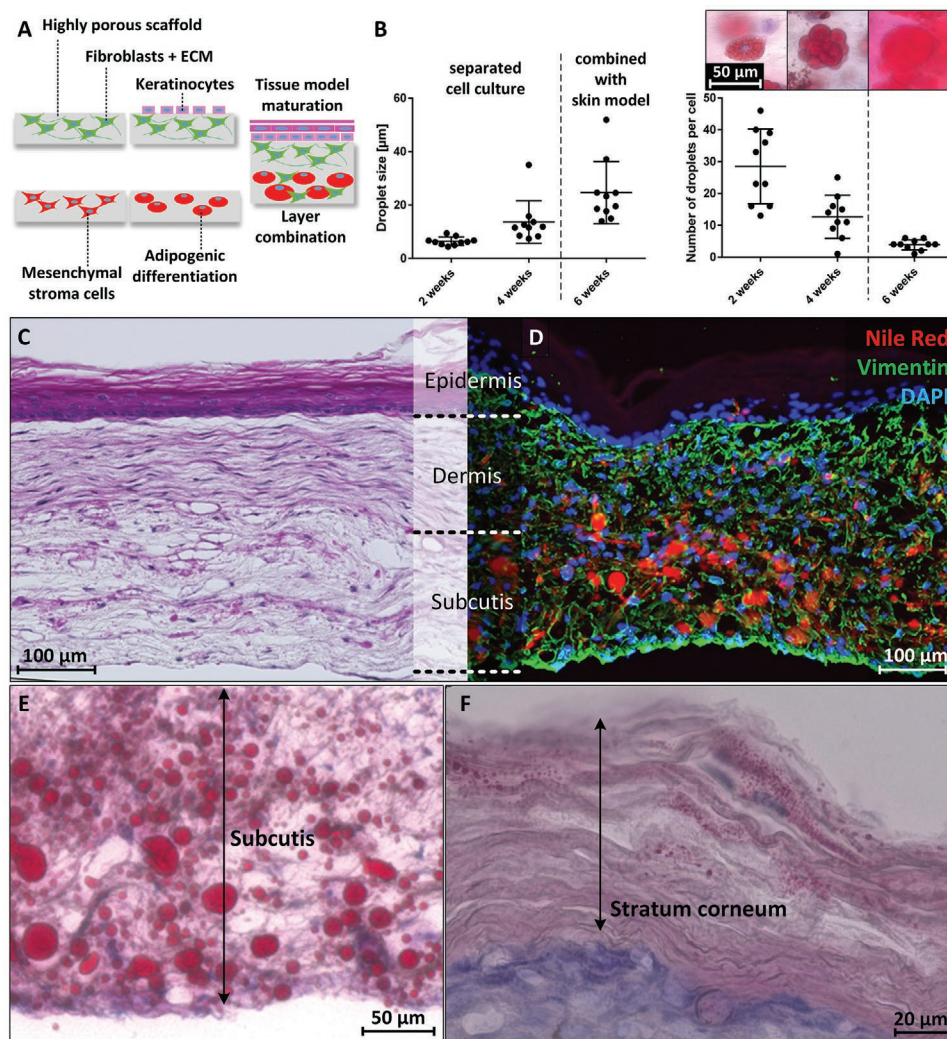


Figure 8. Generation of a three-layered skin model (dermis, epidermis and subcutis) based on the highly porous PA6 fibrous scaffolds. A) Schematic figure of the experimental setup for three-layered skin models. B) Measurement of size and number of oil droplets in the adipogenic differentiated cells ($n = 10$ cells). After 4 weeks of differentiation, the adipose tissue scaffolds were combined with the upper skin model. The insets represent one adipocyte after the indicated differentiation time. C) H&E-stained paraffin section shows the electrospun-fiber-based skin model with epidermis, dermis, and subcutis. Typical for paraffin embedding, the lipids of the adipocytes are removed and appear as holes. D) Fluorescence staining against vimentin (green) and staining of lipids by Nile Red (red) shows the different cellular distributions in the three-layered skin model. E) Combination of HE and Oil Red staining in cryo-sections show the high amount of lipids in the subcutis. F) Visualization of the epidermis and the nanoscaled oil droplets formed in the stratum corneum.

skin equivalents were repeated analogously on the highly porous electrospun PCL scaffolds. After biologization of the highly porous scaffold by 2 weeks of incubation with hDF, the suitability as a skin equivalent was demonstrated by the generation of an epidermal layer on top of it (Figure S6A, Supporting Information). The formation of the dermal part was again analyzed by staining against vimentin (Figure S6B, Supporting Information) and collagen I (Figure S6C, Supporting Information). The comparison with PA6 implies a less homogenous cell and matrix distribution in the dermis of the PCL-based skin equivalent. These differences might be caused by different embedding techniques. Comparable to PA6 scaffolds, hEK cultured on PCL scaffolds showed an epidermis-specific expression of cytokeratin 14 (Figure S6D, Supporting Information) and 10 (Figure S6E, Supporting Information).

The adipogenic differentiation of hMSCs in the PCL scaffold revealed only minor changes in cell morphology (Figure S7A–C, Supporting Information) compared to PA6, in which early differentiating cells had a more roundish shape (Figure S7F,G, Supporting Information). By measuring the oil droplet size (Figure S7D, Supporting Information) and quantity per cell (Figure S7E, Supporting Information) during 6 weeks of adipogenic differentiation, no material-based difference in the differentiation efficiency was detected. Furthermore, no prominent material-dependent influences could be shown for the formation of a three-layered skin equivalent as displayed in Figure S7F in the Supporting Information. The closer look on the epidermis also demonstrated the characteristic oil droplets in the stratum corneum (Figure S7G, Supporting Information).

3. Discussion

The dependence on animal-derived scaffold materials is one of the most challenging pitfalls in the engineering of soft tissues. The most prominent advantages of animal materials are the native protein structures from pico (peptide sequence) over nano/micro (e.g., ECM structure) up to micro/millimeter scale (organ structures, e.g., vascularization),^[39–41] which cannot be replaced by current synthetic alternatives, despite of ethical concerns and production-related disadvantages. Existing substitutes to biological scaffolds such as Puramatrix by Corning, biogelx or 3DProSeed by Ectica Technologies are synthetic hydrogels with highly defined biological properties, whose current prices inhibit the development of voluminous tissues and mass production. Solid-state alternatives, for example sponge-like structures (Alvetex by Repronics) or micro-fibrous structures (MIMETIX by Electrospinning Company; SeedEZ by Lena Biosciences) can supply excellent mechanical stability and high porosity. However, these scaffolds lack many characteristics of native stromal tissues, such as poor intrinsic flexibility and oversized structures. Apart from surface-located interaction molecules like diverse amino acid sequences, the structural imitation, nanofibrous combined with porosity, describes the most critical feature in the design of synthetic 3D scaffolds scaffold. Thereby, the 3D scaffold needs to tolerate or even stimulate native cell–ECM-related interactions such as migration, proliferation, differentiation and structural/biological remodeling. Previously modified electrospinning processes included mainly the introduction of a variety of soluble porogens in between the fibers^[42,43] or subsequent foaming processes,^[44] ice crystal formation^[45] or others,^[46] to improve 3D cellular accessibility of nanofibrous scaffolds for cellular applications. Cumulated, the studies mainly targeted on the generation of pores and disregarded the combination with the more important mesh openings and their stability. In contrast, the scaffolds presented here combine porosity and accessibility as the achieved interconnectivity allows migration of cells from pore to pore, and thereby supports a homogeneous cell distribution throughout the complete scaffold. The generated laminar structure appeared to stabilize the loose fibrous network with the efficient fiber layer separation by the pores. Even when removing the fluid around the scaffold, the pores were able to store a suitable amount of fluid between the fiber layers, preventing a complete structural collapse and thereby facilitating tissue handling and further medium changes during cell culture. Most important, no functional 3D soft tissues based on electrospun scaffolds were generated previously. The production technology of the presented scaffolds also supports a suitable scalability for a good availability and enables the transfer into clinical and preclinical applications. In vivo experiments could show the cell migration into the pores, however, in vitro, cell migration was only improved to a small extent. This can be explained by too dense fiber layers between the porogens and pores. Thus, the fiber density in the fiber layers needs to be drastically reduced, to achieve a stable scaffold accessible for cells. In this study, highly porous 3D fiber scaffolds were generated to minimize the material and fiber density in the scaffold volume, with the aim of suitable synthetic structures addressing all previously defined requirements.

To fulfil basic requirements such as biocompatibility, availability and suitability for electrospinning, the widely applied polymers PA6^[47,48] and PCL^[49] were chosen for this study. The high flexibility of polymer sub-micrometer or nanofibers led to a substantial loss in scaffold volume by capillary forces, when dissolving the porogens, resulting in decreased scaffold porosity. Previous publications demonstrated that simultaneous spinning and porogen integration can hardly achieve the required amounts of porogens for a suitable 3D electrospun scaffold.^[42,50] To overcome this issue, we repetitively paused the spinning process for the addition of particular porogens between the generated fiber layers. By defining the repeating-spinning times, it was possible to control the total porogen proportion and the fiber density in the individual fiber layers, and thereby achieve a defined porosity. Hence, the spinning period describes a critical parameter in 3D fibrous scaffold fabrication, which can be standardized. To comply with the final basic requirement of a standardized fabrication in further developments, the manual porogen integration will be replaced by automated additive processes. Concerning standardization, the application of highly defined and characterized standard polymers, e.g., medical grade, hardly reduces variations in quality and facilitates the implementation of GMP processes.

After removing the porogens in aqueous media, the high porosity led to an effective separation of the thin fiber layers when filled with water, which stabilized the scaffold structure. Unfortunately, the highly porous structure could not be stabilized after porogen removal without fluids, negating most conventional material characterization methods. Independent from the material, the porous scaffolds facilitated a high migration potential for stromal cells, fulfilling the first prerequisite for a biological application. After reaching a certain cellular density inside the 3D structure, the proliferation almost stopped except at the transition from 3D to 2D at the scaffold's surfaces. Gillery et al.^[51] described the attainment of an earlier steady state of cell in 3D environment compared to 2D.

The second biological requirement is the ability for biological remodeling of the 3D scaffold. The degradation of synthetic polymers by cells is not possible, however, matrix remodeling also includes structural adaptations and ECM synthesis as well as the deposition of matrix proteins. The loose fiber assembly allowed hF to move and attach along single fibers, thus leading to a contraction of the whole scaffold. Similar to collagen hydrogels, in which fibroblasts can adapt the material density and mechanical properties by contraction,^[52] the highly porous fiber scaffold structure was remodeled. As nanoindentation can sense material properties similar to cells, the cell free porous scaffold showed a similar Young's modulus like hydrogels,^[53,54] which further increased with cells,^[54] suggesting a similar cellular interaction. Additionally, the simple supplementation of ascorbic acid derivatives fostered the secretion of human specific collagen I in the fiber scaffolds by hF.^[55] Interestingly, the ECM synthesis was significantly reduced in the polyamide scaffolds. The more protein-like or peptide-like amide bonding resulting in a reduced surface protein denaturation compared to highly hydrophobic PCL might be a reason for this result. The promising interactions between fibroblast and the highly porous scaffold as well as the structure of the scaffold comply with almost all requirements as a synthetic replacement for

animal-derived scaffolds in stromal tissue engineering. The population with hdF and the subsequent tissue remodeling results in a biological construct, similar to connective tissue. As the scaffold thickness is currently limited to $\approx 200 \mu\text{m}$ due to the fabrication technique, thicker tissues were achieved by stacking several cell-seeded scaffolds. A prominent application of connective tissue is the engineering of full thickness skin equivalents. hEKs were seeded on top of the dermal part and matured like standard collagen-hydrogel-based skin equivalents.^[56] The formation of a qualitative and functional epidermis showed to our knowledge the first successful generation of a skin equivalent composed of dermis and functional epidermis based on electro-spun scaffolds from synthetic materials. The issue of the epidermal tissue engineering on electrospun scaffolds in previous studies is the rough surface and the lack of functional ECM proteins for cell adhesion and differentiation.^[57] Seeding of tissue-specific hdF beforehand resulted in a biologization of the scaffolds by filling the pores and mesh openings with cells and ECM. The biologization of synthetic scaffolds by fibroblasts for epidermal reconstruction was already described with the scaffold Alvetex.^[14] Nevertheless, the application of the fibrous scaffold morphology in the stromal layer instead of sponge-like structures improved the more tissue-like behavior of the hdF in our study. It is conceivable, that the composition of the synthesized ECM in the scaffold might be controlled by the selection of tissue cell types, such as organ specific fibroblasts, hMSCs, immune cells, endothelial cells,^[58–60] and the applied media supplement composition.^[61–63] This approach could facilitate the generation of a variety of organ specific synthetic-material-based stromal tissues. When applying these biologized scaffolds for tissue engineering, the culture conditions, the cell culture medium and the properties of the scaffold need to be adjusted to the specific organ. For the generation of skin tissue, the culture at the air–liquid interface is a key aspect for the epidermal maturation. The planar surface of the dermal tissue constructs allowed a continuous stable epidermal closure without gaps at the edges and thus allowed the utilization of impedance spectroscopy, a nondestructive technique for epidermal characterization. When comparing the $\text{TEER}_{1000\text{Hz}}$ to reconstructed human epithelium (RHE),^[38] the values of the synthetic-fiber-based skin equivalents measured with the same setup was about 10 times lower. The high ionic diffusion in the porous fiber scaffold compared to the low diffusion cross section and limited lateral diffusion capability of the nanosized porous membrane used for the RHE might explain this large difference. This behavior indicates an amplification of the impedance of RHEs on track etched membranes, while the fibrous model might mimic an improved ionic diffusion in comparison to the in vivo situation. By the achievement of a seamless barrier, the electrospun-fiber-based skin equivalent can be applied for trans-epidermal transport studies. Compared to available in vitro full thickness skin equivalents^[64–66] and even 3D-printed biofabricates,^[67] advantages arise with the utilization of electrospun scaffolds by completely preventing the lateral contraction and the consequence of epidermal gap formation or tissue deformation, as well as by the direct application and handling in a transwell insert.

To increase the complexity of engineered tissues, the highly porous fibrous scaffolds are particularly suited for the assembly

of layered hierarchical tissues. Current studies applied for the hypodermal tissue engineering primarily use isolated mature adipocytes or pre-differentiated hMSCs^[31,68,69] as the combination of hMSCs and hEK and their required media supplementations would negatively influence their differentiation and maturation. Moreover, the complex manufacturing processes and limited availability of matured adipocytes impair the translation. To address this issue, different cell types were cultured and differentiated on separated scaffolds with tailored media compositions, respectively. This cellular pre-maturation prevented the occurrence of dedifferentiation, as soon as the distinct tissues were stacked and culture medium was adjusted to the complete tissue setup. After scaffold stacking, hdF from the middle layer directly started to migrate into the lower subcutaneous layer after combination due to the lower cell density in this part. This behavior consolidated the different stromal tissues and adjusted the cell density and contraction level of both tissue layers. In contrast to previous three-layered skin equivalents^[31,68] where all layers are in direct contact, the lateral contraction could be completely prevented, as the fibers are immobilized at the surrounding insert material.

In further investigations, advanced analysis of the cellular behavior is necessary, like determination of the detailed ECM composition and cellular subtype differentiations. In order to better understand the influence of synthetic 3D fibrous environments on the cellular behavior, a more effective guidance during tissue maturation can be achieved and applied for further specific stromal/organ tissue assembly. Although the high porosity maintains the nutrient supply by diffusion, a high cellular content being accompanied by increased metabolism might limit the obtainable tissue thickness. Therefore, the implementation of vascular structures within the 3D construct is highly interesting/needed in future development. In preparation for clinical applications, comprehensive in vivo studies are required. The most comparable scaffold in the literature^[70] already demonstrated outstanding results as a subcutaneous implant regarding cell migration, neovascularization inside, inflammation and capsule prevention. Furthermore, we also demonstrated the advantages of high porosities of electrospun carbon fibers on the tissue integration subcutaneously.^[35] As both examples already possessed high porosities but quite dense fiber layers, high expectations are generated due to the improved cellular accessibility of the enhanced fibrous structure, as well as the resulting opportunities for animal-free ATMPs.

4. Conclusion

Taken together, this study demonstrates the applicability of highly porous, synthetic, sub-micrometer fiber structures as scaffolds for stromal tissues. Compared to previous 3D spinning approaches, the developed spinning technique could further improve porosity combined with cellular accessibility and structural stability in fluids. The loose fibrous network showed elastic and viscoelastic properties similar to hydrogels and thereby combines the biological relevant microscale mechanical properties of hydrogels with the material availability and production scales of electrospinning. The pores separating fiber

layers initially act as micro-sized 3D environments, which fused together to form stromal tissue by the interactions between scaffold and hF. Concerning cell migration, proliferation and differentiation, the cellular behavior was largely independent from the applied scaffold material/polymer, creating scope exemplarily for various adaptations in polymer degradation/resorption. Thus, bioresorbable materials for implants like ATMPs, or materials for in vitro tissue models with improved chemical stability as an advantage in tissue analysis (paraffin embedding) can be considered in the future. To replace animal-derived materials, the development of 3D tissue models based on these fibrous constructs can address numerous applications as stromal scaffolds. Furthermore, by replacing animal-derived media supplements with human-based or recombinant alternatives, complete animal-free tissue constructs are achievable in the near future. Moreover, the approach of stacking different stromal tissue constructs allowed the efficient generation of a three-layered skin tissue including subdermal, adipose tissue. Thus, this technology might be also applied for other multilayered tissue models with increased complexity.

5. Experimental Section

Ethical Clearance Statement: Primary human epidermal keratinocytes (hEK) and dermal fibroblasts (hF) used in this study were isolated from foreskin biopsies obtained from donors aged between 1 and 3 years under written informed consent of their legal guardians. Mesenchymal stromal cells (hMSCs) were isolated from bone marrow of the femur head of osteoarthritis patients undergoing surgical femur head replacement under written informed consent. The study was conducted according to ethical approval granted by the institutional ethics committee of the Julius-Maximilians-University Würzburg (vote 280/18 and 182/10). Porcine skin was obtained from sacrificed three 6-weeks-old domestic pigs in compliance with the Guide for Care and Use of Laboratory Animals and approved by the local animal protection board.

Electrospinning of Highly Porous Polymer Fiber Scaffolds: The modified electrospinning process for the generation of 3D electro-spun scaffolds was adapted from a previously developed protocol.^[34] A 12% (m/v) solution of polyamide 6 (Sigma-Aldrich, 181 110) or polycaprolactone (Sigma-Aldrich, 440 744) in 1,1,1,3,3,3-hexafluoro-2-propanol (Sigma-Aldrich, 105 228) was spun on a custom-made coaxial electro spinner system.^[71] The distance and voltage was set to 15 cm and 7–9 kV (DC; positive voltage), respectively. Fibers were collected on a rotating target (1600 min⁻¹) resulting in a surface speed of around 9 m s⁻¹ on the rotating collector. To achieve a highly porous structure, the spinning process was halted after 3 min and the scaffold surface on the rotation target was wetted with ethanol (99.8%, Carl Roth, T171.2) and powdered with NaCl particles (Sigma-Aldrich, S7653, milled to a particle diameter between 80 and 125 μm). Therefore, a conventional 50 mL centrifuge tube with 30 holes in the lid (generated by a 1 mm drill) was applied by hand, to homogeneously distribute the particles on the wetted scaffold surface. Within this step, the NaCl particles were dissolved slightly on the surface and increased the adhesion force on the fibers after ethanol evaporation to resist the subsequent centrifugal forces. The total spinning process was finished after 30 repetitions of spinning and embedding of porogens.

Characterization of Highly Porous Polymer Fibrous Scaffolds: To analyze the porous structure in scaffold cross sections, a scaffold was first embedded in paraffin, like biological samples, including an ascending ethanol series from water to xylol. After cutting the paraffin sections, sections were deparaffinized and embedded in Entellan (Merck, 1 079 600 500). Cross sections were visualized by a Keyence microscope BZ-9000 (Germany) using the bright-field mode. To improve the visibility

of the fiber scaffold, images were inverted, followed by an intense adaptation of the brightness and contrast by Fiji-software. The same software was applied to measure the scaffold thickness and pore sizes. The scaffold thickness was measured at 5 different places.

As drying leads to the collapse of the porous structure, no conventional porosity measurement methods could be applied. To calculate the porosity of the scaffolds, the mass fraction of polymer fibers and NaCl of the scaffolds pieces with defined sizes were determined first. This was achieved by measuring the weight of the as-spun scaffold, removing the porogen with water, drying and measuring the weight again. By inclusion of the density of the polymer, the actual polymer mass of the defined scaffold piece as well as the previous measured scaffold thickness, the theoretical porosity of the scaffold in water was calculated.

For imaging the mesh openings, scaffolds were placed in a Petri dish with a glass slide bottom (FluoroDish Cell Culture Dish, World Precision Instruments, FD35-100) containing water. After removal of the NaCl particles, a metal ring ($d = 1.1$ cm) was placed on the fiber scaffold to capture the scaffold directly on the glass slide bottom and to prevent further movements of the fibers during the following microscopy. Imaging was conducted by confocal reflection microscopy with a Leica LSM SP8 (Germany), a laser wavelength of 476 nm and a z-stack depth of 50 μm. The measurement of mesh openings was realized by Fiji software, measuring in total three confocal images and 3 depth levels within these pictures.

Material Preparation for 3D Cell Culture: Electrospun scaffolds were cut in squares of 3 cm edge length and placed in a Petri dish with deionized (DI) water. For each sample, two scaffolds were clamped on top of each other into a cell crown^[96] and washed several times with DI water to remove the NaCl particles. Alternatively, the scaffolds were clamped to a Thincert 12-well transwell insert (Greiner Bio One, Germany) by first removing the poly(ethylene terephthalate) (PET) membrane and fixing the scaffold in place with a silicone tube. Afterward, the scaffolds were gamma sterilized under submerged (DI water) conditions. As remaining solvent residues in the fibers are harmful for cells during culture, scaffolds were incubated in PBS for at least 4 days before cell seeding.

Cell Isolation and Culture: Human epithelial keratinocytes (hEK) were isolated from human foreskin as previously described.^[66] Briefly, the epidermis is separated from dermis after incubation in dispase (2 U mL⁻¹, Gibco, Carlsbad, USA, 17105-041). Following a digestion step with trypsin the cells are isolated from the epidermal pieces via mechanical disruption of the tissue. Cells were expanded in EpiLife basal medium supplemented with HKGS (Human Keratinocyte Growth Supplement) and 1% penicillin/streptomycin (Fisher Scientific GmbH, Schwerte, Germany). Media was changed three times per week. Cell type and purity was determined by FACS analysis of Cytokeratin 14 (Figure S8, Supporting Information).

Human dermal fibroblasts (hF) were isolated after the removal of the epidermis by collagenase (500 U mL⁻¹, SERVA Electrophoresis GmbH, Germany, 17 454) digestion of the dermis as previously described.^[65] The cells were expanded in Dulbecco's modified Eagle medium (DMEM) supplemented with 10% fetal calf serum (FCS) (Gibco) and 1× Pen/Strep (PAA Laboratories, P11-010) with medium changes three times per week.

hMSCs were isolated from bone marrow of the femur head of patients suffering from osteoarthritis undergoing surgical femur head replacement.^[72] Cells were cultured in DMEM/F12 (Gibco, 31 331 028) + 10% FCS (Bio&Sell) + 5 ng mL⁻¹ human basic fibroblast growth factor (hbFGF) (R&D systems) 1× Pen/Strep with three media changes per week. For adipose tissue cultures, hMSCs were used in passage 3–5.

FACS Analysis of Human Primary Keratinocytes: Flow cytometry was performed using the BD Accuri (BD; Heidelberg, Germany) with 100.000 cells per sample. Cells were harvested and fixated for 20 min using the BD Fixation/Permeabilization Buffer (BD; Heidelberg). Afterward, cells were washed twice with BD Perm/Wash buffer (BD; Heidelberg) and incubated with an anti-keratin 14-[fluorescein isothiocyanate (FITC)] antibody (LSBio; Seattle, WA, USA) or a control (Mouse IgG3 Isotype Control [FITC]; LSBio; Seattle) for 30 min at 4 °C. Antibodies were diluted 1:100 in 2 × 10⁻³ M EDTA and 5% BSA in PBS⁻.

Cells were then washed three times with 2×10^{-3} M EDTA and 5% BSA in PBS⁻ and stored protected from light until analysis. Data were analyzed with FlowJo Software (v10).

Culture of hDF: Prior to cell seeding, scaffolds clamped in cell crowns, were placed in 12-well plates (TPP Techno Plastik Products AG). hDF were seeded on scaffolds with a cell density of 30 000 cells per cm² in 1.5 mL expansion medium (DMEM, 10% FCS, Pen/Strep). After two days of culture, the medium was supplemented with either 100×10^{-6} or 500×10^{-6} M ascorbic acid 2-phosphate (Sigma-Aldrich, A8960). Culture was conducted for two and four weeks with medium changes three times per week.

Quantitative Hydroxyproline Assay: The assay was adapted by Kesava Reddy et al.^[73] Briefly, samples were placed in 2 mL reaction vessels with 500 μ L 6 M HCl (Carl Roth, Germany) and hydrolyzed for 20 h at 95 °C. As the low pH influences the assay, the hydrolyzed samples were dried and dissolved again in 200 μ L DI water. For the assay, 35 μ L of the samples and a hydroxy-proline standard were transferred in a 96-well plate in duplicates. Hydroxy-proline standard was prepared by dissolving L-hydroxy-proline (Sigma-Aldrich, Germany) in DI water with a concentration range between 20 and 160 μ g mL⁻¹. Afterward, 75 μ L of a chloramine-T reagent was added to each specimen followed by a 20 min incubation at RT. The chloramine-T reagent was prepared by dissolving 1.27 g chloramine-T trihydrate (Sigma-Aldrich, Germany) in 20 mL *n*-propanol (Merck Millipore, Germany) and stocked up 100 mL with acetate-citrate buffer. As the subsequent coloration step. 75 μ L of Ehrlich's reagent (1.5 g 4-(dimethylamino)-benzaldehyde (Sigma-Aldrich, Germany) in 6.6 mL of *n*-propanol and 3.3 mL 70% perchloric acid (both Carl Roth, Germany)) was added to each well and incubated at 60 °C for 60 min after sealing the well plate with a Microseal "B" PCR Plate Sealing Film (Bio-Rad, United Kingdom). The following measurement of the coloration intensity was performed by a photometer Infinite M200 PRO (Tecan, Germany) at 570 nm.

Culture of hMSC and Adipogenic Differentiation: hMSCs used for the generation of 3D adipose tissue modelling were characterized according to the minimal criteria stated by the International Society for Cellular Therapy.^[74] Briefly, the isolated cells were analyzed for the ability to adhere on plastic surfaces, a required surface marker-profile and the differentiation capacities toward the adipogenic, chondrogenic and osteogenic lineage.^[75] Like the 3D culture of hDF, electrospun scaffolds were placed in 12-well plates. Following, hMSCs were seeded on the scaffolds with a cell density of 100 000 cells per cm². To achieve a suitable cell density within the whole 3D scaffold, cells were first cultured for 2 weeks in hMSC expansion medium. Subsequently, medium was changed to an adipogenic differentiation medium (ADM) containing DMEM (Gibco, 61 965 026), 10% FCS, dexamethasone (Sigma-Aldrich, D4902), insulin (Sigma-Aldrich, I9278), indomethacin (Sigma-Aldrich, I8280), 3-isobutyl-1-methylxanthine (IBMX, AppliChem, A0695), D-glucose (Sigma-Aldrich, G8769) and lipid mixture (Sigma-Aldrich, L0288) for enhanced lipid accumulation.^[76] Differentiation was performed for three weeks with medium changes three times per week.

Mechanical Characterization: For biologization, highly porous scaffolds were treated as described in a previous section (3D culture of hDF) and cultured for up to 4 weeks with 500×10^{-6} M Asc. For preparing decellularized samples, 4 weeks hDF cultured samples as well as porcine skin ($\approx 1 \times 5$ cm; removed subcutis) were treated according to Di Meglio et al. protocol 4.^[77] Briefly, the samples were incubated under agitation in 1% sodium dodecyl sulfate (SDS, Carl Roth GmbH, CN30.4) solution (DI water) for 18 hours with changing the fluid three times. Afterward, the samples were incubated for 30 min in 1% Triton X-100 (Carl Roth GmbH, 3051) and subsequently washed with PBS⁻ (containing 1 U Pen/Strep) for 2 days. Until usage samples were stored for up to 3 days at 4 °C.

Tensile Testing: Stress-strain measurements were performed in a Zwick universal testing machine (Zwick Roell, Ulm, Germany/100 N or 10 kN load cell), at ambient temperature as well as humidity. Before clamping, a slice of ≈ 3 mm was cut off for thickness determination, by paraffin embedding, slicing and microscopic measuring. All samples

were clamped in the testing machine directly from the storing solution (PBS⁻) without any drying treatment. As adhesive support, a rough abrasive paper was fixed in the clamping unit for all electrospun samples. Before starting the measurement, the breath and clamping distance was determined by a caliper square. The stress strain measurement was performed by a separation speed of 50 mm min⁻¹. The measured force was converted into mechanical stress using the estimated cross section. The Young's modulus (tensile modulus) was determined in the linear region of the stress-strain curve (Figure S3, Supporting Information). Four stress strain diagrams of each tissue were analyzed for the evaluation of the Young's modulus, ultimate tensile stress and failure stress ratio.

Nanoindentation: Samples were placed wrinkle-free in 6-well plates, weighted with metal rings ($d = 1.1$ cm) and covered with 4 mL PBS⁻. Measurements were performed with a PAVONE Nanoindenter (Optics11, Amsterdam, The Netherlands) and a probe with 0.26 N m⁻¹ cantilever stiffness and 50 μ m spherical tip radius resulting in an approximately contact radius of 20 μ m at 8 μ m indentation. Measurements were conducted using the controlled indentation mode and a depth of 8 μ m with an initial relaxation time of 15 s before starting DMA measurement using the following protocol: I. 0.5 Hz—5 periods—Amplitude 100 nm—Relaxation 2 s; II. 1 Hz—5 periods—Amplitude 100 nm—Relaxation 2 s; III. 2 Hz—5 periods—Amplitude 100 nm—Relaxation 2 s; IV. 4 Hz—10 periods—Amplitude 100 nm—Relaxation 2 s; V. 10 Hz—20 periods—Amplitude 100 nm—Relaxation 2 s; VI. 40 Hz—80 periods—Amplitude 100 nm—Relaxation 2 s. All samples were measured with a 3 \times 3 matrix scan with 100 μ m distance, resulting in 9 measurement points per scaffold. Young's modulus was defined by hertz fit of the indentation curve and the viscoelastic parameters determined using the PAVONE corresponding software DataViewer V2.5 (Optics11).

Generation of a Two-Layered Skin Model (Dermis and Epidermis) Based on the Highly Porous Fibrous Scaffolds: The dermal part of the skin was generated as described in section 3D culture of hDF. Briefly, two scaffolds were clamped in a cell crown, seeded with hDF and cultured for 2 weeks in hDF expansion medium containing 500×10^{-6} M ascorbic acid 2-phosphate. After two weeks, the generated tissues of two cell crowns were combined by stacking on top of each other and clamped in one cell crown. Alternatively, two scaffolds were clamped onto a 12-Well Thincert transwell insert, seeded with hDF and cultured for 2 weeks in hDF expansion medium containing 500×10^{-6} M ascorbic acid 2-phosphate.

Afterward, hEK were seeded on top of the tissue with a cell density of 600 000 cells per cm² in Epilife basal medium supplemented with HKGS, 1% penicillin/streptomycin and 1.44×10^{-3} M CaCl₂. One day later, cell crowns were transferred in a 6-well plate and the tissue was set to airlift culture by adding 2.5 mL Epilife basal medium supplemented with HKGS, 1% penicillin/streptomycin, 1.44×10^{-3} M CaCl₂, 73 μ g mL⁻¹ L-ascorbic acid 2-phosphate and 10 ng mL⁻¹ keratinocyte growth factor. Following, tissue maturation was performed for three weeks with medium changes three times per week.

Impedance Spectroscopy: For impedance spectroscopy skin models were placed between two nanostructured titanium nitride electrodes of a custom-made measuring system, which was previously described.^[78,79] The space surrounding the models and inside the culture inserts were filled with Epilife medium, supplemented with 1% penicillin/streptomycin and 1.44×10^{-3} M calcium chloride to achieve electrical coupling with the electrodes. Afterward, 40 logarithmically distributed measuring points in a frequency ranging from 1 Hz to 100 kHz were measured with the LCR HiTESTER 3522-50 (HIOKI E.E. Corporation, Japan).

Generation of a Three-Layered Skin Model (Dermis, Epidermis, and Subcutis) Based on the Highly Porous Fibrous Scaffolds: For the generation of a three-layered skin model, the upper skin part and the adipogenic part were cultured separately. First, the engineering of the adipogenic part was started as described above. Tissues were cultured for 5 weeks. In parallel but two weeks delayed, the engineering of the upper skin part was initiated as described in the paragraph above. After one week of airlift culture, the two-layered skin model composed of epidermis and dermis was complemented with the subcutaneous tissue by clamping

two generated adipose tissues under one upper skin part, respectively. Tissue maturation was performed for three weeks with medium changes (same medium as in the two-layered skin model) three times per week.

Histology and Immunohistology: Paraffin sections were stained by a standard H&E staining procedure. To achieve a combined staining of Oil Red and H&E, stainings were performed in a row. The critical step here was the embedding of the samples, as a hydrophilic embedding removes the eosin staining and hydrophobic embedding the Oil Red (and the PCL-fibers). To overcome this, samples were embedded with a hydrophilic mounting medium (Aquatex, Merck, 108 562) and immediately analyzed by a Keyence microscope BZ-9000 before the eosin staining was washed out.

For immunohistology, following primary antibodies and concentrations were applied: rabbit-anti-vimentin (abcam, ab92547) 1:2000; rabbit-anti-CD90 (abcam, ab92574) 1:200; rabbit-anti- β -Tubulin (abcam, ab78078) 1:1000; rabbit-anti-Glucose transporter 4 (Glut4) (abcam, ab654) 1:1000; mouse-anti-Cytokeratin 10 (DAKO Cytomation, M7002) 1:2000; rabbit-anti-Cytokeratin 14 (Sigma-Aldrich, HPA023040) 1:1000; rabbit-anti-Collagen I (abcam, ab138492) 1:1000; rabbit-anti-collagen IV (abcam, ab6586) 1:600; mouse-anti-laminin 5 (abcam, ab78286) 1:100; rabbit-anti-Ki67 (abcam, ab15580) 1:100; lipophilic fluorescent dye Nile Red (Sigma-Aldrich, N3013, 1 μ g mL⁻¹). All primary antibodies were incubated on the samples overnight. The next day, the samples were washed 3 times in PBS + Tween-20 (0.5%, Sigma-Aldrich, P1379) for 5 min, following the incubation of the secondary antibody for 1 h with a dilution of 1:200. The following secondary antibodies were applied: donkey-anti-mouse-488 (Invitrogen, A-21202), donkey-anti-mouse-555 (Invitrogen, A-31570), donkey-anti-rabbit-488 (Invitrogen, A-21206), donkey-anti-rabbit-555 (Invitrogen, A-31572). Fluorescence microscopy was performed either with the Keyence microscope BZ-9000 or a Leica LSM SP8 (Germany).

Statistics: After data were tested for normality, statistical significance was determined by analysis of variance (ANOVA). At a *p*-value below 0.05, results were treated as significantly different.

Supporting Information

Supporting Information is available from the Wiley Online Library or from the author.

Acknowledgements

This work was partially funded by the German Federal Ministry of Education and Research: grant agreement number 13N12971-ETface. The authors thank the Fraunhofer Project Center for Stem Cell Process Engineering for the provision of their nanoindentation device. Furthermore, the authors thank Keldan Chapman for proof-reading the manuscript.

Open Access funding enabled and organized by Projekt DEAL.

Conflict of Interest

The authors declare the following competing financial interest(s): a patent for highly porous nanofiber scaffolds for stromal tissues was submitted by the Fraunhofer ISC, Patent 102 021 200 128.9, Hochporöse Nanofaservliese als Trägerstruktur für stromales Gewebe.

Data Availability Statement

The data that support the findings of this study are available from the corresponding author upon reasonable request.

Keywords

3D scaffolds, electrospinning, highly porous materials, multilayered skin, stromal tissues

Received: August 27, 2021

Revised: December 14, 2021

Published online: January 21, 2022

- [1] G. Pennarossa, S. Arcuri, T. de Iorio, F. Gandolfi, T. A. L. Brevini, *Int. J. Mol. Sci.* **2021**, 22, 830.
- [2] R. Ramezankhani, S. Torabi, N. Minaei, H. Madani, S. Rezaeiani, S. N. Hassani, A. P. Gee, M. Dominici, D. N. Silva, H. Baharvand, E. Hajizadeh-Saffar, *Front. Cell Dev. Biol.* **2020**, 8, 547653.
- [3] *3D Cell Culture Market Size, Share & Trends Analysis Report By Technology (Scaffold-free, Scaffold-based), By Application (Cancer, Stem Cell Research), By End Use, By Region, And Segment Forecasts, 2021–2028. Report ID: GVR-1-68038-091-0*, Grand View Research, San Francisco, CA, USA **2021**.
- [4] *Advanced Therapy Medicinal Products Market Size, Share & Trends Analysis Report By Therapy Type (CAR-T, Gene, Cell, Stem Cell Therapy), By Region (North America, Europe, APAC, ROW), And Segment Forecasts, 2021–2028. Report ID: GVR-3-68038-855-8*, Grand View Research, San Francisco, CA, USA **2021**.
- [5] P. M. J. Bos, L. Geraets, L. de Wit-Bos, M. Heringa, J. van Engelen, *ALTEX - Altern. Animal Exp.* **2020**, 37, 395.
- [6] R. M. Nerem, A. Sambanis, *Tissue Eng.* **1995**, 1, 3.
- [7] B. P. Chan, K. W. Leong, *Eur. Spine J.* **2008**, 17, 467.
- [8] T. Wagner, M. Gschwandtner, A. Strajeriu, A. Elbe-Bürger, J. Grillari, R. Grillari-Voglauer, G. Greiner, B. Golabi, E. Tschachler, M. Mildner, *Sci. Rep.* **2018**, 8, 13434.
- [9] G. Dotalbano, S. Toumpaniari, A. Popov, P. Duan, J. Chen, K. Dalgarno, W. E. Scott, A. M. Ferreira, *Mater. Sci. Eng., C* **2018**, 91, 236.
- [10] F. Morshedloo, A. B. Khoshfetrat, D. Kazemi, M. Ahmadian, *J. Biomed. Mater. Res., Part B* **2020**, 108, 2950.
- [11] M. W. McCrory, D. Bousalisa, S. Mobiniabc, Y. H. Songad, C. E. Schmidt, *Acta Biomater.* **2020**, 111, 1.
- [12] F. Pati, D.-W. Cho, in *3D Cell Culture: Methods and Protocols* (Ed: Z. Koledova), Springer New York, New York **2017**, pp. 381–390.
- [13] D. S. Hill, N. D. P. Robinson, M. P. Caley, M. Chen, E. A. O'Toole, J. L. Armstrong, S. Przyborski, P. E. Lovat, *Mol. Cancer Ther.* **2015**, 14, 2665.
- [14] M. Roger, N. Fullard, L. Costello, S. Bradbury, E. Markiewicz, S. O'Reilly, N. Darling, P. Ritchie, A. Määttä, I. Karakesisoglou, G. Nelson, T. von Zglinicki, T. Dicolandrea, R. Isfort, C. Bascom, S. Przyborski, *J. Anat.* **2019**, 234, 438.
- [15] B. V. Slaughter, S. S. Khurshid, O. Z. Fisher, A. Khademhosseini, N. A. Peppas, *Adv. Mater.* **2009**, 21, 3307.
- [16] V. A. Chimisso, M. A. Garcia, S. Yorulmaz Avsar, I. A. Dinu, C. G. Palivan, *Molecules* **2020**, 25, 4090.
- [17] S. Ye, J. W. B. Boeter, M. Mihajlovic, F. G. Steenbeek, M. E. Wolferen, L. A. Oosterhoff, A. Marsee, M. Caiazzo, L. J. W. Laan, L. C. Penning, T. Vermond, B. Spee, K. Schneeberger, *Adv. Funct. Mater.* **2020**, 30, 2000893.
- [18] S. J. Hollister, *Adv. Mater.* **2009**, 21, 3330.
- [19] B. S. Spearman, N. K. Agrawal, A. Rubiano, C. S. Simmons, S. Mobini, C. E. Schmidt, *J. Biomed. Mater. Res., Part A* **2020**, 108, 279.
- [20] X. Meng, P. Leslie, Y. Zhang, J. Dong, *SpringerPlus* **2014**, 3, 80.
- [21] G. Rijal, W. Li, *Biomaterials* **2016**, 81, 135.
- [22] S. Imayama, I. M. Braverman, *Anat. Rec.* **1988**, 222, 115.
- [23] P. Friedl, K. Maaser, C. E. Klein, B. Niggemann, G. Krohne, K. S. Zänker, *Cancer Res.* **1997**, 57, 2061.

- [24] A. Kim, C. Zhou, N. Lakshman, W. M. Petroll, *Exp. Cell Res.* **2012**, 318, 741.
- [25] L. E. Flynn, *Biomaterials* **2010**, 31, 4715.
- [26] G. Agmon, K. L. Christman, *Curr. Opin. Solid State Mater. Sci.* **2016**, 20, 193.
- [27] J. van Smeden, J. A. Bouwstra, *Curr. Probl. Dermatol.* **2016**, 49, 8.
- [28] E. E. Kershaw, J. S. Flier, *J. Clin. Endocrinol. Metab.* **2004**, 89, 2548.
- [29] C. M. Alexander, I. Kasza, C.-L. E. Yen, S. B. Reeder, D. Hernandez, R. L. Gallo, C. A. B. Jahoda, V. Horsley, O. A. MacDougald, *J. Lipid Res.* **2015**, 56, 2061.
- [30] R. W. Grant, V. D. Dixit, *Obesity* **2015**, 23, 512.
- [31] F. F. Schmidt, S. Nowakowski, P. J. Kluger, *Front. Bioeng. Biotechnol.* **2020**, 8, 388.
- [32] B. Huber, A. Link, K. Linke, S. A. Gehrke, M. Winnefeld, P. J. Kluger, *Tissue Eng., Part C* **2016**, 22, 756.
- [33] J. Xue, T. Wu, Y. Dai, Y. Xia, *Chem. Rev.* **2019**, 119, 5298.
- [34] T. Weigel, T. Pfister, T. Schmitz, M. Jannasch, S. Schürlein, R. A. Hijailan, H. Walles, J. Hansmann, *BioNanoMaterials* **2017**, 18, 2.
- [35] T. Weigel, T. Schmitz, T. Pfister, S. Gaetzner, M. Jannasch, R. Al-Hijailan, S. Schürlein, S. Suliman, K. Mustafa, J. Hansmann, *Sci. Rep.* **2018**, 8, 14545.
- [36] C. Moll, J. Reboredo, T. Schwarz, A. Appelt, S. Schürlein, H. Walles, S. Nietzer, *J. Visualized Exp.* **2013**, 78, 50460.
- [37] K. Nomura, T. Sugawara, T. Sato, D. Sawamura, I. Hashimoto, Y. Sugita, J. Uitto, *Arch. Dermatol. Res.* **1994**, 286, 408.
- [38] L. Kieseewetter, L. Littau, H. Walles, A. R. Boccaccini, F. Groeber-Becker, *Biosens. Bioelectron.* **2019**, 142, 111555.
- [39] J. Schanz, J. Pusch, J. Hansmann, H. Walles, *J. Biotechnol.* **2010**, 148, 56.
- [40] M. Schweinlin, S. Wilhelm, I. Schwedhelm, J. Hansmann, R. Rietscher, C. Jurowich, H. Walles, M. Metzger, *Tissue Eng., Part C* **2016**, 22, 873.
- [41] A. T. Stratmann, D. Fecher, G. Wangorsch, C. Göttlich, T. Walles, H. Walles, T. Dandekar, G. Dandekar, S. L. Nietzer, *Mol. Oncol.* **2014**, 8, 351.
- [42] J. Wu, Y. Hong, *Bioact. Mater.* **2016**, 1, 56.
- [43] J. Rnjak-Kovacina, A. S. Weiss, *Tissue Eng., Part B* **2011**, 17, 365.
- [44] Y. Chen, M. Shafiq, M. Liu, Y. Morsi, X. Mo, *Bioact. Mater.* **2020**, 5, 963.
- [45] M. Simonet, O. D. Schneider, P. Neuenschwander, W. J. Stark, *Polym. Eng. Sci.* **2007**, 47, 2020.
- [46] M. Vong, F. J. Diaz Sanchez, A. Keirouz, W. Nuansing, N. Radacsi, *Mater. Des.* **2021**, 208, 109916.
- [47] R. Nirmala, R. Navamathavan, S.-J. Park, H. Y. Kim, *Nano-Micro Lett.* **2014**, 6, 89.
- [48] F. Zomer Volpato, F. Ramos, L. S. , A. Motta, C. Migliaresi, *J. Bioact. Compat. Polym.* **2011**, 26, 35.
- [49] M. J. Mochane, T. S. Motsoeneng, E. R. Sadiku, T. C. Mokhena, J. S. Sefadi, *Appl. Sci.* **2019**, 9, 2205.
- [50] J. Nam, Y. Huang, S. Agarwal, J. Lannutti, *Tissue Eng.* **2007**, 13, 2249.
- [51] P. Gillery, A. Laperre, F. Coustry, F.-X. Maquart, J.-P. Borel, *FEBS Lett.* **1992**, 296, 297.
- [52] D. Karamichos, R. A. Brown, V. Mudera, *J. Biomed. Mater. Res., Part A* **2007**, 83, 887.
- [53] S. Huth, S. Sindt, C. Selhuber-Unkel, *PLoS One* **2019**, 14, 0220281.
- [54] M. D. A. Norman, S. A. Ferreira, G. M. Jowett, L. Bozec, E. Gentleman, *Nat. Protoc.* **2021**, 16, 2418.
- [55] O. Hakimi, R. Poulson, D. Thakkar, C. Yapp, A. Carr, *Oxid. Antioxid. Med. Sci.* **2014**, 3, 119.
- [56] J. Lange, F. Weil, C. Riegler, F. Groeber, S. Rebhan, S. Kurdyn, M. Alb, H. Kneitz, G. Gelbrich, H. Walles, S. Mielke, *Biotechnol. J.* **2016**, 11, 1352.
- [57] A. Rossi, L. Wistlich, K.-H. Heffels, H. Walles, J. Groll, *Adv. Healthcare Mater.* **2016**, 5, 1939.
- [58] H. O. Ozguldez, J. Cha, Y. Hong, I. Koh, P. Kim, *Biomater. Res.* **2018**, 22, 32.
- [59] T. Weigel, J. Brennecke, J. Hansmann, *Materials* **2021**, 14, 1378.
- [60] Y. Mao, T. Hoffman, A. Wu, R. Goyal, J. Kohn, *J. Mater. Sci.: Mater. Med.* **2017**, 28, 100.
- [61] S. Edgar, B. Hopley, L. Genovese, S. Sibilla, D. Laight, J. Shute, *Sci. Rep.* **2018**, 8, 10474.
- [62] J. Y. Hsu, M. Y. Hsu, T. Sorger, M. Herlyn, E. M. Levine, *In Vitro Cell. Dev. Biol.: Anim.* **1999**, 35, 647.
- [63] L. M. Boyd, J. Chen, V. B. Kraus, L. A. Setton, *Spine* **2004**, 29, 2217.
- [64] K. Ackermann, S. Lombardi Borgia, H. C. Korting, K. R. Mewes, M. Schäfer-Korting, *Skin Pharmacol. Physiol.* **2010**, 23, 105.
- [65] M. Jannasch, F. Groeber, N. W. Brattig, C. Unger, H. Walles, J. Hansmann, *Exp. Parasitol.* **2015**, 150, 22.
- [66] A. Rossi, A. Appelt-Menzel, S. Kurdyn, H. Walles, F. Groeber, *J. Visualized Exp.* **2015**, 96, 52576.
- [67] K. Derr, J. Zou, K. Luo, M. J. Song, G. S. Sittampalam, C. Zhou, S. Michael, M. Ferrer, P. Derr, *Tissue Eng., Part C* **2019**, 25, 334.
- [68] S. E. L. Vidal, K. A. Tamamoto, H. Nguyen, R. D. Abbott, D. M. Cairns, D. L. Kaplan, *Biomaterials* **2019**, 198, 194.
- [69] E. Bellas, M. Seiberg, J. Garlick, D. L. Kaplan, *Macromol. Biosci.* **2012**, 12, 1627.
- [70] J. Jiang, S. Chen, H. Wang, M. A. Carlson, A. F. Gombart, J. Xie, *Acta Biomater.* **2017**, 68, 237.
- [71] D. Radakovic, J. Reboredo, M. Helm, T. Weigel, S. Schürlein, E. Kupczyk, R. G. Leyh, H. Walles, J. Hansmann, *PLoS One* **2017**, 12, 0185916.
- [72] K. M. Pawelec, D. Confalonieri, F. Ehlicke, H. A. van Bortel, H. Walles, S. G. J. M. Kluijtmans, *J. Biomed. Mater. Res., Part A* **2017**, 105, 1856.
- [73] G. Kesava Reddy, C. S. Enwemeka, *Clin. Biochem.* **1996**, 29, 225.
- [74] M. Dominici, K. Le Blanc, I. Mueller, I. Slaper-Cortenbach, F. Marini, D. Krause, R. Deans, A. Keating, D. Prockop, E. Horwitz, *Cytotherapy* **2006**, 8, 315.
- [75] C. Kleinhans, R. R. Mohan, G. Vacun, T. Schwarz, B. Haller, Y. Sun, A. Kahlig, P. Kluger, A. Finne-Wistrand, H. Walles, J. Hansmann, *Biotechnol. J.* **2015**, 10, 1727.
- [76] C. Malkmus, S. Jawahar, N. Tricoche, S. Lustigman, J. Hansmann, *PLoS Neglected Trop. Dis.* **2020**, 14, 0008503.
- [77] F. Di Meglio, D. Nurzynska, V. Romano, R. Miraglia, I. Belviso, A. M. Sacco, V. Barbato, M. Di Gennaro, G. Granato, C. Maiello, S. Montagnani, C. Castaldo, *Tissue Eng., Part C* **2017**, 23, 525.
- [78] F. Groeber, L. Engelhardt, S. Egger, H. Werthmann, M. Monaghan, H. Walles, J. Hansmann, *Pharm. Res.* **2015**, 32, 1845.
- [79] T. Schmitz, M. Schweinlin, R. T. Kollhoff, L. Engelhardt, C. Lotz, F. Groeber-Becker, H. Walles, M. Metzger, J. Hansmann, *ACS Appl. Nano Mater.* **2018**, 1, 2284.